

Numerical investigation on performance of electrohydrodynamic thruster with needle-ring electrode

Chun-Yan Wang(王春岩), Hu-Lin Huang(黄护林), Hao Li(李灏), Tian-Tian Chen(陈田田), and Xi-Jing Hu(胡锡精)
Citation: Chin. Phys. B, 2026, 35 (**3**): 035205. DOI: 10.1088/1674-1056/adf829
http://cpb.iphy.ac.cn; http://iopscience.iop.org/cpb

What follows is a list of articles you may be interested in

Experimental and numerical analyses of electrohydrodynamic force according to air pressure

Rong-Hui Quan(全荣辉), Bo Wang(王博), and Yun-Jia Yao(姚韵佳)
Chin. Phys. B, 2023, 32 (**6**): 065201. DOI: 10.1088/1674-1056/acac11

Fractal microstructure of Ag film via plasma discharge as SERS substrates

Xue-Fen Kan(阚雪芬), Cheng Yin(殷澄), Zhuang-Qi Cao(曹庄琪), Wei Su(苏巍), Ming-Lei Shan(单鸣雷), and Xian-Ping Wang(王贤平)
Chin. Phys. B, 2021, 30 (**12**): 125201. DOI: 10.1088/1674-1056/ac0693

Review on ionization and quenching mechanisms of Trichel pulse

Anbang Sun(孙安邦), Xing Zhang(张幸), Yulin Guo(郭雨林), Yanliang He(何彦良), and Guanjun Zhang(张冠军)
Chin. Phys. B, 2021, 30 (**5**): 055207. DOI: 10.1088/1674-1056/abd75d

Enhancement of corona discharge induced wind generation with carbon nanotube and titanium dioxide decoration

Jianchun Ye(叶建春), Jun Li(李俊), Xiaohong Chen(陈晓红), Sumei Huang(黄素梅), Wei Ou-Yang(欧阳威)
Chin. Phys. B, 2019, 28 (**9**): 095202. DOI: 10.1088/1674-1056/ab33ed

Characteristics and underlying physics of ionic wind in dc corona discharge under different polarities

Tongkai Zhang(张桐恺), Yu Zhang(张宇), Qizheng Ji(季启政), Ben Li(李犇), Jiting Ouyang(欧阳吉庭)
Chin. Phys. B, 2019, 28 (**7**): 075202. DOI: 10.1088/1674-1056/28/7/075202

Numerical investigation on performance of electrohydrodynamic thruster with needle-ring electrode

Chun-Yan Wang(王春岩)[1], Hu-Lin Huang(黄护林)[1,†], Hao Li(李灏)[1], Tian-Tian Chen(陈田田)[1], and Xi-Jing Hu(胡锡精)[2]

[1] *Laboratory of Aerospace Entry Descent and Landing Technology, College of Astronautics, Nanjing University of Aeronautics and Astronautics, Nanjing* 211106, *China*
[2] *Beijing Institute of Control and Electronic Technology, Beijing* 100038, *China*

(Received 16 May 2025; revised manuscript received 30 June 2025; accepted manuscript online 6 August 2025)

The electrohydrodynamic (EHD) thruster is a propulsion system characterized by its propellant-free operation. This paper employs a plasma chemical model to systematically investigate three critical parameters affecting EHD propulsion performance: oxygen concentration, secondary electron emission coefficient (SEEC), and voltage polarity. Results show that optimizing the nitrogen-to-oxygen concentration ratio from 4:1 to 5:1 under positive corona discharge enhances the thrust-to-power ratio by 41.3%. Furthermore, increasing the SEEC from 0.001 to 0.01 produces significant performance improvements, with thrust increasing by 34.5% and thrust-to-power ratio surging by 142.2%. Notably, negative corona discharge exhibits substantially reduced efficiency, as the accumulation of positive charges near the emitter electrode induces aerodynamic resistance, resulting in thrust values less than 1% of those achieved in positive discharge configurations.

Keywords: electrohydrodynamic (EHD) thruster, corona discharge, oxygen concentration, secondary electron emission coefficient, voltage polarity

PACS: 52.65.–y, 52.75.Di, 47.85.L–, 82.33.Xj

DOI: 10.1088/1674-1056/adf829 **CSTR:** 32038.14.CPB.adf829

1. Introduction

Near-space environments hold significant strategic importance for intelligence, surveillance, and reconnaissance (ISR) applications, with the investigation of long-endurance propulsion systems for near-space platforms emerging as a major area of interest.[1] The electrohydrodynamic (EHD) thruster demonstrates distinct advantages in near-space microjet applications,[2,3] including structural simplicity, zero-noise operation and combustion-free operation without propellant requirements[4–8] — advantages over conventional propulsion technologies. A notable advancement was achieved by Xu's fixed-wing aircraft prototype,[8] which successfully validated EHD propulsion technology through flight experiments. However, in terms of operational range, endurance duration, and payload capacity, current EHD aircraft still show significant performance gaps when compared to conventional aircraft of similar size. As a result, significant research is still required to develop novel strategies for improving EHD thruster performance.

The EHD thruster typically employs multiple emitter-collector pairs, operating through corona discharge-induced ionic wind propulsion.[9] Performance characteristics vary significantly across different electrode configurations due to structural diversity. Among prevalent designs, the wire-to-cylinder configuration demonstrates enhanced propulsion performance in positive corona discharge regimes through optimized air pressure and inter-electrode spacing.[10] To enhance thrust, the design of EHD thrusters can be optimized by adjusting electrode arrangements, for instance, parallel electrode alignment[11] or incorporating intermediate electrodes.[5] To expand the ion-receiving area and prevent discharge from the collector electrode, Jewell developed a novel wire-grid electrode structure.[12] Daniel also developed a wire-grid EHD thruster incorporating a silicon tube electrode bracket, demonstrating significant application potential for micro air vehicles.[13] Subsequent studies on needle-net configurations revealed that airflow velocity can be enhanced through channel radius expansion,[14] while thrust exhibits quadratic growth with increasing applied voltage.[15] The needle-ring structure has several advantages over traditional electrode geometries, including structural simplicity, axial symmetry, and minimal flow disturbance.[16] By using this setup to study multi-stage series performance in negative corona discharges, Rickard[17] demonstrated that airflow acceleration happens inside the cavity when electric field forces exceed viscous friction. Granados' simulation studies[18–21] predicted EHD propulsion performance in near-space environments, yet they only considered pure nitrogen, pure oxygen, or pure argon, failing to account for atmospheric gas mixtures.

Based on recent research regarding EHD thrusters, the following conclusions can be drawn: (i) While diverse elec-

[†]Corresponding author. E-mail: hlhuang@nuaa.edu.cn

© 2026 Chinese Physical Society and IOP Publishing Ltd. All rights, including for text and data mining, AI training, and similar technologies, are reserved.

trode configurations have been extensively studied, there remains a research gap regarding the propulsion performance of needle-ring structures. (ii) Existing studies predominantly focus on EHD thruster characteristics under standard atmospheric conditions. (iii) Systematic comparisons between positive and negative corona discharges are lacking, and the effects of oxygen concentration and secondary electron emission coefficient (SEEC) on the EHD thruster are not considered. (iv) Current numerical simulations often neglect gas discharge processes, while existing simplified models (Kaptzov hypothesis[22] and three-particle model[23]) exhibit limitations in both completeness and accuracy. To address these research gaps, the EHD thruster with needle-ring electrode is investigated in this paper. Meanwhile, the plasma chemical model is adopted, which considers the major particle species and chemical reactions in near-space air ionization, and analyze in detail the propulsion performance under varying SEEC, nitrogen-oxygen concentration ratios, and voltage polarities.

2. Calculation model

2.1. Physical model

The EHD thruster comprises a needle-ring electrode pair and an insulating shell, as shown in Fig. 1. The needle acts as the emitter electrode, while the ring electrode serves as the collector electrode. During operation, corona discharge primarily occurs near the emitter electrode. For positive corona discharge, the emitter electrode maintains a higher potential than the collector electrode. Positively charged ions generated by air ionization are drawn to the collector electrode by this potential difference. These ions collide with neutral molecules, transferring momentum that drives airflow into the inlet and expels it through the outlet. When the voltage polarity is reversed for negative corona discharge, the direction of ion movement becomes entirely opposite to that of the positive discharge scenario. Consequently, the airflow within the thruster is driven by negatively charged ions. By definition, the electrode with the higher potential is termed the anode, and the other is referred to as the cathode.

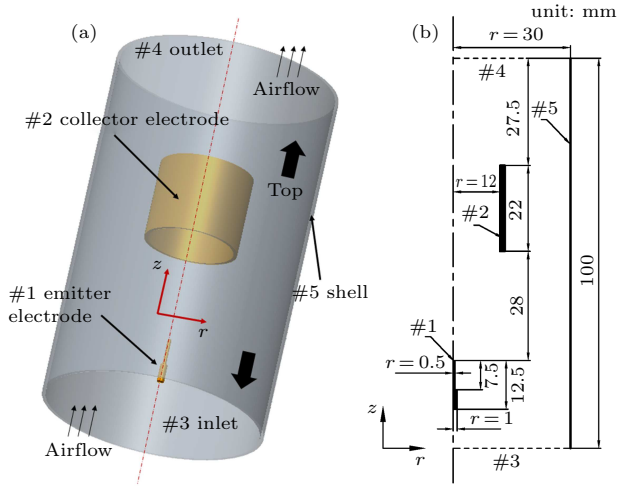


Fig. 1. Schematic diagram of the EHD thruster, (a) three-dimensional (3D) rotating structure diagram, (b) two-dimensional (2D) cross-section diagram.

2.2. Governing equations

2.2.1. Electron transport equations

The species transport equation for electron density and the conservation equation for electron density are[18,19]

$$\frac{\partial}{\partial t}(n_{\mathrm{e}}) + \nabla \cdot \boldsymbol{\Gamma}_{\mathrm{e}} = R_{\mathrm{e}} - (\boldsymbol{\mu} \cdot \nabla) n_{\mathrm{e}}, \tag{1}$$

$$\frac{\partial}{\partial t}(n_{\mathrm{e}}) + \nabla \cdot \boldsymbol{\Gamma}_{\varepsilon} + \boldsymbol{E} \cdot \boldsymbol{\Gamma}_{\mathrm{e}} = R_{\varepsilon} - (\boldsymbol{\mu} \cdot \nabla) n_{\varepsilon}, \tag{2}$$

$$\boldsymbol{\Gamma}_{\mathrm{e}} = -n_{\mathrm{e}}(\boldsymbol{\mu}_{\mathrm{e}} \cdot \boldsymbol{E}) - \nabla(\boldsymbol{D}_{\mathrm{e}} n_{\mathrm{e}}), \tag{3}$$

$$\boldsymbol{\Gamma}_{\varepsilon} = -n_{\varepsilon}(\boldsymbol{\mu}_{\varepsilon} \cdot \boldsymbol{E}) - \nabla(\boldsymbol{D}_{\varepsilon} n_{\varepsilon}), \tag{4}$$

where t is time, n_{e} is electron density, $\boldsymbol{\Gamma}_{\mathrm{e}}$ is electron flux, R_{e} is electron source term, $\boldsymbol{u}$ is velocity vector, n_{ε} is electron energy density, Γ_{ε} is electron energy flux, $\boldsymbol{E}$ is electric field, R_{ε} is electron energy source term, $\boldsymbol{\mu}_{\mathrm{e}}$ is electron mobility, $\boldsymbol{D}_{\mathrm{e}}$ is electron diffusion coefficient, μ_{ε} is electron energy mobility, $\boldsymbol{D}_{\varepsilon}$ is electron energy diffusion coefficient.

The electron transport coefficients satisfy the Einstein relation,[24] and the electron mobility is obtained from the LXCat database,[25]

$$\boldsymbol{D}_{\mathrm{e}} = \boldsymbol{\mu}_{\mathrm{e}} T_{\mathrm{e}} k_{\mathrm{B}}, \tag{5}$$

$$\boldsymbol{D}_{\varepsilon} = \boldsymbol{\mu}_{\varepsilon} T_{\mathrm{e}} k_{\mathrm{B}}, \tag{6}$$

$$\mu_{\varepsilon} = \frac{5}{3}\boldsymbol{\mu}_{\mathrm{e}}, \tag{7}$$

$$T_{\mathrm{e}} = \frac{2\bar{\varepsilon}}{3k_{\mathrm{B}}}, \tag{8}$$

where T_{e} is electron temperature, k_{B} is Boltzmann constant, $\bar{\varepsilon}$ is mean electron energy.

The source term in Eq. (9) is the sum of the M reaction rates that cause the electron density to increase or decrease, and the source term in Eq. (10) is the sum of the electron collision reaction rates multiplied by the energy loss or gain of the considered P kinds of inelastic electron collision reactions,[18]

$$R_{\mathrm{e}} = \sum_{j=1}^{M} x_j k_j N_0 n_{\mathrm{e}}, \tag{9}$$

$$R_{\varepsilon} = \sum_{j=1}^{P} x_j k_j N_0 n_{\mathrm{e}} \Delta\varepsilon_j, \tag{10}$$

where j is the j-th reaction, x_j is mole fraction of target species for reaction j, k_j is rate coefficient for reaction j, N_0 is number density of neutral species, $\Delta\varepsilon_j$ is energy lost or obtained in reaction j.

The reaction rate coefficients can be determined by electron energy distribution function (EEDF) $f(\varepsilon)$ and collision

cross section $\sigma_j(\varepsilon)$.[26] The cross-section data of electron collision reactions (reactions 1–5 in Table 1) are select from LXCat database.[25]

$$k_j = \left(\frac{2q}{m_e}\right)^{1/2} \int_0^\infty \varepsilon \sigma_j(\varepsilon) f(\varepsilon)\, \mathrm{d}\varepsilon, \tag{11}$$

$$f(\varepsilon) = \bar{\varepsilon}^{-3/2} \beta_1 \exp\left(-(\varepsilon\beta_2/\bar{\varepsilon})\right), \tag{12}$$

$$\beta_1 = \Gamma(5/2)^{3/2} \Gamma(3/2)^{-5/2}, \tag{13}$$

$$\beta_2 = \Gamma(5/2) \Gamma(3/2)^{-1}, \tag{14}$$

where q is unit charge, m_e is electron mass.

2.2.2. Heavy species transport equations

The mass fraction transport equations of heavy species are as follows:[27]

$$\rho \frac{\partial}{\partial t}(w_k) + \rho(\boldsymbol{u}\cdot\nabla) w_k = \nabla\cdot\boldsymbol{\Gamma}_k + R_k, \tag{15}$$

$$\boldsymbol{\Gamma}_k = \rho w_k \boldsymbol{V}_k, \tag{16}$$

$$R_k = M_k \sum_{j=1}^{N} \upsilon_{kj} r_j, \tag{17}$$

where ρ is air density, w_k is mass fraction of species k, $\boldsymbol{\Gamma}_k$ is diffusion flux vector of species k, R_k is source term of species k, M_k is molecular mass of species k, υ_{kj} is stoichiometric matrix, r_j is reaction rate of reaction j.

To calculate the multi-component diffusion rate $\boldsymbol{V}_k$ in Eq. (16), COMSOL Multiphysics software provides two distinct diffusion models: the mixture-averaged model and Fick's law. Both models satisfy all mass conservation criteria and have significantly lower computational costs compared to the full Maxwell–Stefan equations. However, Fick's law is a simpler diffusion model with lower accuracy than the mixture-averaged model. Therefore, the mixture-averaged model was selected for this research.

2.2.3. Poisson equations

The Poisson equations are adopted to calculate the electrostatic field affected by the space charge density,

$$-\nabla\cdot\varepsilon_0\varepsilon_r\nabla V = \rho_e, \tag{18}$$

$$\boldsymbol{E} = -\nabla V, \tag{19}$$

$$\rho_e = q\left(\sum_{k=1}^{N} Z_k n_k - n_e\right), \tag{20}$$

where ε_0 is vacuum dielectric constant, ε_r is relative dielectric constant, ρ_e is space charge density, V is electric potential, Z_k is charge number of species k, n_k is number density of species k.

The current generated by gas discharge is calculated by Sato equation[28]

$$I = \frac{e}{V}\iint 2\pi r(-\mu_e \boldsymbol{E} n_e - \boldsymbol{D}_e\nabla n_e + \mu_p \boldsymbol{E} n_p - \boldsymbol{D}_p\nabla n_p - \mu_n \boldsymbol{E} n_n - \boldsymbol{D}_n\nabla n_n)\cdot\boldsymbol{E}_L\, \mathrm{d}r\mathrm{d}z, \tag{21}$$

where I is current, r is radius of the thruster, μ_p is positive ion mobility, n_p is positive ion number density, $\boldsymbol{D}_p$ is positive ion diffusion coefficient, μ_n is negative ion mobility, $\boldsymbol{D}_n$ is negative ion diffusion coefficient, n_n is negative ion number density, $\boldsymbol{E}_L$ is Laplacian electric field.

2.2.4. Flow control equations

The airflow is assumed to be viscous and laminar since the Reynolds number falls within the range of 1.3–5.4 ($u \approx 2$ cm/s–10 cm/s). This assumption aligns with the fundamental characteristics of EHD flow and is widely adopted in current research.[22] The electric field force $\boldsymbol{F}$ is used in conjunction with the Navier–Stokes equations to represent the flow characteristics and the plasma chemical model. Furthermore, the flow is assumed to be in thermal equilibrium, as the heat generated by corona discharge can be ignored[14,16]

$$\rho\nabla\cdot\boldsymbol{u} = 0, \tag{22}$$

$$\rho\frac{\partial\boldsymbol{u}}{\partial t} + \rho(\boldsymbol{u}\cdot\nabla)\boldsymbol{u} = -\nabla p + \nabla\cdot[\mu(\nabla\boldsymbol{u} + (\nabla\boldsymbol{u})^T)] + \boldsymbol{F}, \tag{23}$$

$$\boldsymbol{F} = -\rho_e\nabla V, \tag{24}$$

where p is pressure, μ is dynamic viscosity, T is gas temperature.

2.2.5. Propulsion performance

According to the characteristics of EHD thrusters, the ions generated in the corona discharge process is accelerated by the electric field force and transfer momentum to the ambient fluid.[14] This momentum coupling phenomenon can induce ionic wind and produce thrust in the direction opposite to ion movement.[8] Hence, the total thrust can be determined by the velocity profile at the outlet section as a function of radial distance.[20]

$$F_T = 2\pi\rho\int_0^{R_d} r u_z^2\, \mathrm{d}r, \tag{25}$$

where F_T is thrust, R_d is radius of the collector electrode, u_z is z-direction velocity.

Thrust efficiency can be measured by the ratio of thrust generated by the system to power consumption,[15] named the thrust-to-power ratio,[29]

$$\eta = F_T/(V_e\cdot I), \tag{26}$$

where η is thrust-to-power ratio, V_e is electrode voltage.

2.3. Plasma chemical model

To accurately simulate the behavior of different gases during air ionization, a plasma chemical model[30] is employed, which including 12 species (e, O, O_2, O_3, N_2^+, N_4^+, O_2^+, O_4^+, $O_2^+N_2$, O_2^-, O^-, N_2) and 26 reactions (listed in Table 1). This model is widely recognized as effective and has been commonly used in current plasma research.[31,32] According to

Eq. (8), electron energy (ε) is correlated with electron temperature (T_e), and the rate coefficients for reactions 1–10 in Table 1 are also determined by T_e. Consequently, the single-temperature model,[23] which only accounts for gas temperature (T), cannot accurately predict these rate coefficients. Notably, Table 1 lacks quenching reactions of excited-state molecules; thus, the plasma chemical model proposed in this paper is unsuitable for simulating arc discharge processes involving significant thermal energy generation. Furthermore, the inclusion of numerous reaction equations inevitably leads to a multiple-fold increase in computational time.

Table 1. Important reaction processes in air corona discharge.

Number	Reaction	Rate coefficient	$\Delta\varepsilon$ (eV)
1	$e+N_2 \Rightarrow e+N_2$	$\sigma_j(\varepsilon)$	1.0
2	$e+O_2 \Rightarrow e+O_2$	$\sigma_j(\varepsilon)$	1.0
3	$e+N_2 \Rightarrow 2e+N_2^+$	$\sigma_j(\varepsilon)$	15.6
4	$e+O_2 \Rightarrow 2e+O_2^+$	$\sigma_j(\varepsilon)$	12.06
5	$e+O_2 \Rightarrow O+O^-$	$\sigma_j(\varepsilon)$	3.6
6	$2e+N_2^+ \Rightarrow e+N_2$	$5.651\times10^{-27}T_e^{-0.8}$	–
7	$e+N_2^+ +N_2 \Rightarrow 2N_2$	$6.07\times10^{-34}T_e^{-2.5}$	–
8	$e+O_4^+ \Rightarrow 2O_2$	$1.4\times10^{-12}\,(300/T_e)^{0.5}$	–
9	$e+O_2^+ \Rightarrow 2O$	$2.42\times10^{-13}\,(300/T_e)$	–
10	$e+2O_2 \Rightarrow O_2+O_2^-$	$2\times10^{-41}\,(300/T_e)$	–
11–12	$N_2^+ +N_2+M \Rightarrow N_4^+ +M$	5×10^{-41}	–
13	$N_4^+ +O_2 \Rightarrow O_2^+ +2N_2$	2.5×10^{-16}	–
14	$N_2^+ +O_2 \Rightarrow O_2^+ +N_2$	$1.04\times10^{-15}T^{-0.5}$	–
15	$2N_2+O_2^+ \Rightarrow N_2O_2^+ +N_2$	$8.1\times10^{-38}T^{-2}$	–
16	$N_2O_2^+ +N_2 \Rightarrow 2N_2+O_2^+$	$14.6T^{-5.3}\exp(-2357/T)$	–
17	$N_2O_2^+ +O_2 \Rightarrow O_4^+ +N_2$	1×10^{-15}	–
18–19	$O_2^+ +O_2+M \Rightarrow O_4^+ +M$	$2.04\times10^{-34}T^{-3.2}$	–
20	$O_4^+ +O_2^- \Rightarrow 3O_2$	1×10^{-13}	–
21–22	$O_4^+ +O_2^- +M \Rightarrow 3O_2+M$	2×10^{-37}	–
23–24	$O_2^+ +O_2^- +M \Rightarrow 2O_2+M$	2×10^{-37}	–
25–26	$O+O_2+M \Rightarrow O_3+M$	2.5×10^{-46}	–

In Table 1, $M = O_2$, N_2. The unit of two-body reaction rate coefficient is m^3/s, and that of three-body reaction rate coefficient is m^6/s.

2.4. Boundary conditions and calculation schemes

The boundary conditions are detailed in Table 2,[27] where the electrodes are modeled as metal materials and the shell is modeled as a dielectric. The interaction between electrons and the walls (the surfaces of electrodes and shell) is governed by a balance of incident fluxes.[18] A DC voltage is applied to the emitter electrode, and an RC series coupling circuit is employed to prevent electrode arcing.[20] The plasma voltage stabilizes within 1 ms and exerts negligible impact on the steady-state characteristics of EHD thrusters. The collector electrode is grounded (set to zero potential). A zero-charge boundary condition is applied at the shell to ensure no charge accumulation on its surface. Meanwhile, a zero-charge boundary condition is employed to maintain no free charge accumulation at the boundary (see #3–#5 in Fig. 1). This condition is commonly used to simulate grounded configurations or systems with equipotential surfaces. To prevent backflow, the inlet pressure is initially set to ambient pressure (10 Torr, 1 Torr = 1.33322×10^2 Pa) and maintained at or above this pressure throughout the calculation process.[21] The outlet pressure is 10 torr, and the velocity of the airflow on the wall is zero.

In Table 2, P_0 is ambient pressure, $v_{e,th}$ is thermal velocity of electrons, γ is secondary electron coefficient, $\boldsymbol{\Gamma}_i$ is flux of positive ions i on the wall, $R_{surf,k}$ is the surface rate of species k, c_k is concentration of species k.

Table 2. Boundary conditions.

Name	Equations	Number
Dc voltage	V_e	#1
Ground	$V=0$	#2
Insulation	$-\boldsymbol{n}\cdot\boldsymbol{\Gamma}_e=0$	
	$-\boldsymbol{n}\cdot\boldsymbol{\Gamma}_\varepsilon=0$	#3,4
	$-\boldsymbol{n}\cdot\boldsymbol{\Gamma}_k=0$	
Zero charge	$-\boldsymbol{n}\cdot\boldsymbol{D}=0$	#3,4,5
Pressure-inlet	$p=p_0$	#3
Pressure-outlet	$p=p_0$	#4
Wall	$-\boldsymbol{n}\cdot\boldsymbol{\Gamma}_e=\left(\frac{1}{2}v_{e,th}n_e\right)-\sum\gamma(\boldsymbol{\Gamma}_i\cdot\boldsymbol{n})$	
	$-\boldsymbol{n}\cdot\boldsymbol{\Gamma}_\varepsilon=\left(\frac{5}{6}v_{e,th}n_\varepsilon\right)-\sum\gamma\varepsilon(\boldsymbol{\Gamma}_i\cdot\boldsymbol{n})$	#1,2,5
	$-\boldsymbol{n}\cdot\boldsymbol{\Gamma}_k=M_kR_{surf,k}+M_kc_kZ_k\mu_k(\boldsymbol{E}\cdot\boldsymbol{n})$	
	$\times[Z_k\mu_k(\boldsymbol{E}\cdot\boldsymbol{n})>0]$	
	$\boldsymbol{u}=0$	

Some species can collide with the electrodes and the shell to generate other species, with the types of surface reactions detailed in Table 3. Specifically, secondary electrons are produced by the bombardment of positive ions on the electrodes. The average energy of these secondary electron is set to 5 eV,[18] which aligns with the typical operating condition of plasma actuators. The calculation results are verified to agree with the qualitative observations from experiments.[24]

Table 3. Surface reaction.

Number	Equations
1	$N_2^+ \Rightarrow N_2$
2	$O_2^+ \Rightarrow O_2$
3	$N_2O_2^+ \Rightarrow N_2+O_2$
4	$N_4^+ \Rightarrow 2N_2$
5	$O_4^+ \Rightarrow 2O_2$
6	$O_2^- \Rightarrow O_2$
7	$O^- \Rightarrow 0.5O_2$
8	$O \Rightarrow 0.5O_2$

The rates of surfaces reactions are expressed as

$$R_{surf,k}=\left(\frac{\gamma_f}{1-\gamma_f/2}\right)\frac{1}{4\,(\Gamma_{tot})^m}\sqrt{\frac{8RT}{\pi M_n}}\prod_{k=1}^{Q}c_k, \tag{27}$$

where γ_f is sticking coefficients, Γ_{tot} is total flux, m is the reaction order minus 1, R is gas constant.

In Table 5, ζ is concentration ratio N_2:O_2.

The simulation domain is a two-dimensional (2D) axisymmetric cylindrical space,[27] and COMSOL Multiphysics software is applied to simulate the EHD performance. The

time-stepping method employs the implicit backward differentiation formulas (BDF), renowned for its stability. Meanwhile, the maximum BDF order is set to 2 with a maximum step size of 10^{-7} s to enhance the robustness of the system. However, this low-order method may induce a degree of damping effect. The parallel sparse direct solver (PARDISO) is utilized, due to its good robustness and high computational speed. The constant parameters and calculation variables are listed in Tables 4 and 5, respectively. The SEEC depends on the electrode material and is varied within the range of 0.001–0.01.[33,34] To investigate the influence mechanism of gas composition on the EHD thruster, the nitrogen-to-oxygen concentration ratio employed in this study ranges from 4:1 (standard atmospheric environment) to 5:1 (laboratory conditions). The initial density of charged species meets the electrical neutrality conditions, and the initial electron density is 1×10^{8} m^{-3}. The initial electron density has been confirmed to only speed up the process of air ionization and cannot change the discharge characteristics.[30,35]

Table 4. Constant parameters in the calculation process.

Parameter	Value	Unit
ε_0	$8.854187817\times10^{-12}$	F/m
ε_r	1	1
T_0	300	K
p_0	10	Torr
ρ	1.53×10^{-2}	kg/m^3

Table 5. Calculation variables for different cases.

Number	V_e (kV)	γ	ζ
Case 1	3	0.01	4:1
Case 2	3	0.01	5:1
Case 3	3	0.001	4:1
Case 4	−3	0.01	4:1

2.5. Grid independence verification

To ensure calculation accuracy and reduce computational time, the grid division scheme adopts refined grids in the boundary layer while keeping other regions relatively sparse. Table 6 presents the results of grid independence verification. Meshes M1 to M4 are progressively refined, and comparison results based on mesh M4 are provided. When using mesh M3, the relative thrust error is 0.15% and the relative current error is 0.36%, indicating that mesh M3 fully meets the required calculation accuracy.

Table 6. Results of grid independence verification.

Mesh	M1	M2	M3	M4
Grids	85108	132161	180324	237675
F (mN)	6.45×10^{-6}	6.41×10^{-6}	6.36×10^{-6}	6.35×10^{-6}
ΔF (%)	1.55	0.93	0.15	0
I (mA)	2.83×10^{-3}	2.79×10^{-3}	2.77×10^{-3}	2.76×10^{-3}
ΔI (%)	2.4	1.07	0.36	0

2.6. Program verification

It is necessary to ensure that the calculation model is established correctly, as the accuracy of the selected model has been validated numerous times and is widely used in current research.[22,35] The present distributions of electric potential and velocity are compared with the results from the literature,[20] as shown in Figs. 2 and 3, respectively. The present thrust is 10.96 nN, and the thrust-to-power ratio is 20.4 μN/W; the relative errors to the literature results are 0.5% and 6.8%, respectively. Therefore, the present results are consistent with those in the literature, verifying the validity of the calculation program. Specifically, the slight discrepancies between the present results and the literature results in Fig. 3 mainly arise from differences in the ion swarm data. The ion swarm data adopted in this research are sourced from reference,[36] which are widely used in related studies.

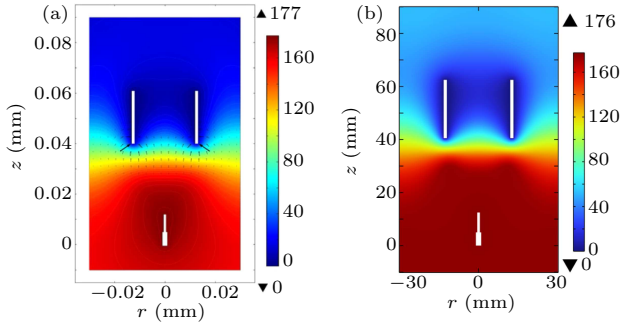


Fig. 2. The spatial distribution of electric potential (in unit V) from (a) literature results,[18] (b) present results.

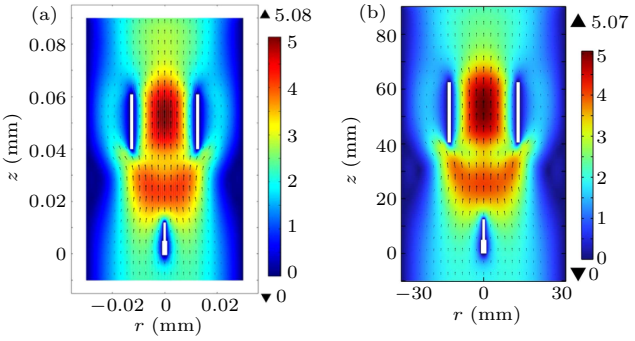


Fig. 3. The spatial distribution of airflow velocity (in unit cm/s) from (a) literature results,[18] (b) present results.

3. Results and discussion

The characteristics of the EHD thruster are analyzed during the stable stage of discharge, as the effects of current fluctuations in the initial stage have negligible impacts on the propulsion performance.

3.1. The characteristics of charged species and electric fields

Electrons are the most critical charged species for initiating gas ionization reactions. Their direct participation in approximately 50% of the chemical reactions occurring in air

discharge systems underpins their dominant role (reactions 1–10, Table 1). The spatial distribution of electron density under various operating parameters is presented in Fig. 4. As illustrated in Fig. 4(a), the electron population is predominantly concentrated near the collector electrode in positive corona discharge configurations. This spatial distribution arises from two complementary mechanisms: First, electrons are neutralized on the surface of the emitter electrode due to electrostatic force. Second, sustained electron generation occurs through surface-mediated chemical reactions at the collector electrode (reactions 1–5, Table 3).

Comparing Figs. 4(a) and 4(b) reveals that the electron density between the emitter and collector electrodes increases as the ζ is adjusted from 4:1 to 5:1. This improvement primarily stems from a twofold rise in electron collision reaction rates (see Table 1, entries 3–4) near the electrode surfaces, which coincides with a decrease in oxygen concentration. This observed phenomenon aligns with established literature findings,[20–22] where comparative studies demonstrate significantly higher electron densities in pure nitrogen environments compared to pure oxygen systems. Such consistency with prior research not only validates our calculation methodology but also reinforces the reliability of our key findings.

As evident from Figs. 4(a) and 4(c), the average electron density increases by 27.7% (from 2.02 $\times 10^{11}$ 1/m^3 to 2.58$\times 10^{11}$ 1/m^3) as γ increases from 0.001 to 0.01. Meanwhile, the dominant electron distribution region undergoes a substantial modification. The underlying mechanisms can be explained as follows: (i) During air discharge, positive ions generated are neutralized through electron interactions. (ii) With a lower SEEC value, more positive ions are transported to the top of the collector electrode, reducing the neutralization rate of positive ions at the bottom. (iii) The accumulation of positive ions on the collector surface strengthens the local electric field, which intensifies electron collision reactions (as described in Eq. (18)). (iv) Newly generated electrons from these collisions accumulate around the collector axis due to electrostatic repulsion from the electrode itself.

However, unlike the positive corona discharge observed in Fig. 4(a), when the applied voltage polarity is switched to negative, electrons accumulate near the emitter electrode, as shown in Fig. 4(d). This phenomenon arises from two key mechanisms: (I) electrons are primarily generated around the emitter electrode via electron collision reactions and surface reactions; (II) simultaneously, electrons are neutralized at the collector electrode surface.

Based on the above-calculated electron density results (see Fig. 4), the density of positive ions along the axis of the EHD thruster is displayed in Fig. 5. Given that oxygen molecules require less energy to ionize than nitrogen molecules, O_2^+ and O_4^+ are evidently the dominant positive ions compared to other ion species. Notably, O_4^+ exhibits the highest abundance among positive ions, as it can still be generated through collisions between O_2^+ and other charged particles (see entries 18–19 in Table 1). The crucial role of oxygen ionization in corona discharge has been well-established in numerous studies,[24,31,37] and ion distribution trends similar to those presented here have also been observed in some experiments.[31] These findings further validate the accuracy of the calculation method used in this research.

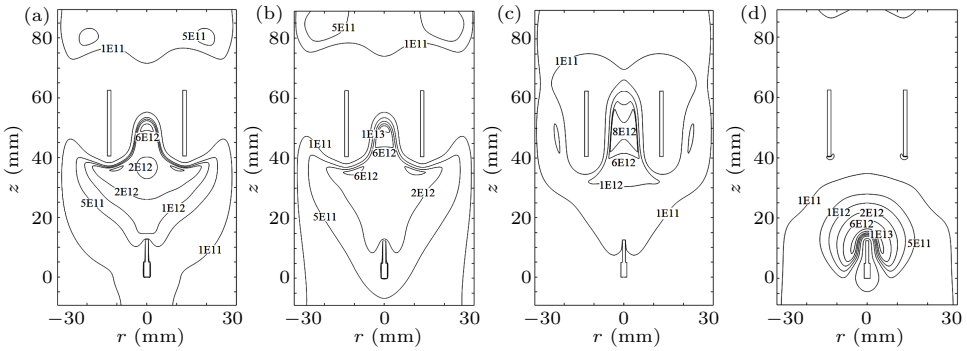


Fig. 4. The spatial distribution of electron density (in unit 1/m^3) at (a) $V_e = 3$ kV, $\gamma = 0.01$, $\zeta = 4:1$; (b) $V_e = 3$ kV, $\gamma = 0.01$, $\zeta = 5:1$; (c) $V_e = 3$ kV, $\gamma = 0.001$, $\zeta = 4:1$; (d) $V_e = -3$ kV, $\gamma = 0.01$, $\zeta = 4:1$.

The negative ion density along the axis of the EHD thruster is shown in Fig. 6. It can be clearly observed that the number density of O^- is greater than that of O_2^- by two orders of magnitude across varying calculation parameters. This discrepancy arises because the dissociativeattachment reaction rate for O^- generation is significantly higher than the O_2^- generation (see entries 5 and 10 in Table 1). Notably, the relative abundance of these two negative ions (see Fig. 6) is only evident under low-pressure conditions. At atmospheric pressure, however, the reaction rate of negative ions is significantly altered, leading to a higher number density of O_2^- than that of O^-.[32]

In order to further investigate the properties of charged species under low-pressure conditions, figure 7 presents the spatial distribution of charge density under different parameters, and figure 8 illustrates the ion reaction rates along the

EHD thruster's axis. In the positive corona discharge configuration, specifically, positive charges occupy the remaining thruster volume (drift area), whereas negative charges primarily accumulate near the emitter electrode tip (ionization region), as shown in Fig. 7(a). Notably, the ionization region is significantly smaller in spatial extent compared to the drift region.

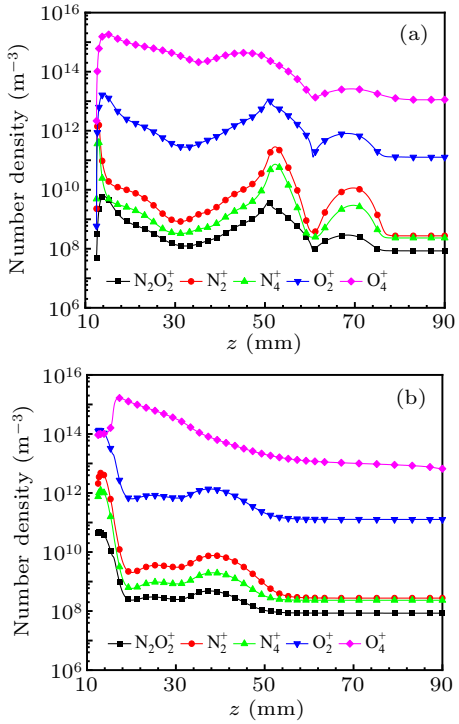


Fig. 5. The positive ions density along the axis of the EHD thruster at (a) $V_e = 3$ kV, $\gamma = 0.01$, $\zeta = 4:1$; (b) $V_e = -3$ kV, $\gamma = 0.01$, $\zeta = 4:1$.

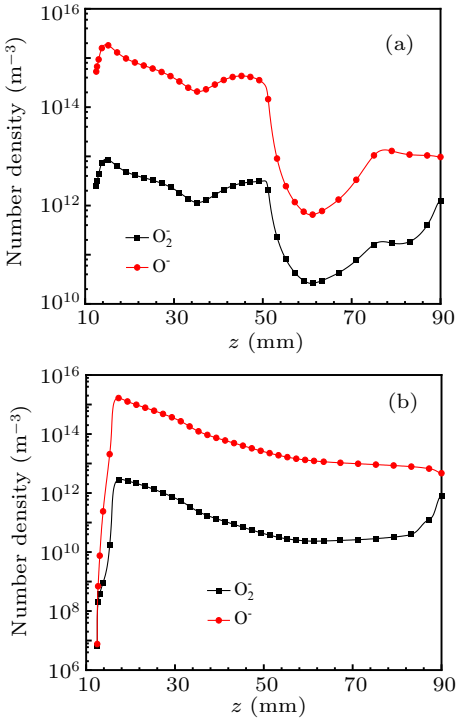


Fig. 6. The negative ions density along the axis of the EHD thruster at (a) $V_e = 3$ kV, $\gamma = 0.01$, $\zeta = 4:1$; (b) $V_e = -3$ kV, $\gamma = 0.01$, $\zeta = 4:1$.

From Figs. 7(a) and 7(b), it can be observed that the maximum charge density in the drift region decreases from 4.09×10^{-5} C/m^3 to 3.49×10^{-5} C/m^3 as the ζ changes from 4:1 to 5:1. This trend can be interpreted through the following points: (i) According to Eq. (20), charge density is related to the reaction rates of electrons and ions. (ii) In the corresponding thruster region, the electron density is two orders of magnitude lower than the ion density. (iii) With the decrease in oxygen concentration, the positive ion reaction rate in the drift region increases by a factor of 1.55 (see the lines for case 1 and case 2 in Fig. 8(a)), while the negative ion reaction rate remains nearly unchanged (see the curves for case 1 and case 2 in Fig. 8(b)).

The charge density around the axis of collector electrode can be diminished with the reduction of SEEC range from 0.01 to 0.001, as depicted in Figs. 7(a) and 7(c). This phenomenon arises because the positive ion reaction rate (see the lines corresponding to case 1 and case 3 in Fig. 8(a)) along the z-axis of the collector electrode within the range of 40 mm–60 mm diminishes, while the negative ion reaction rate (see the curves for case 1 and case 3 in Fig. 8(b)) increases.

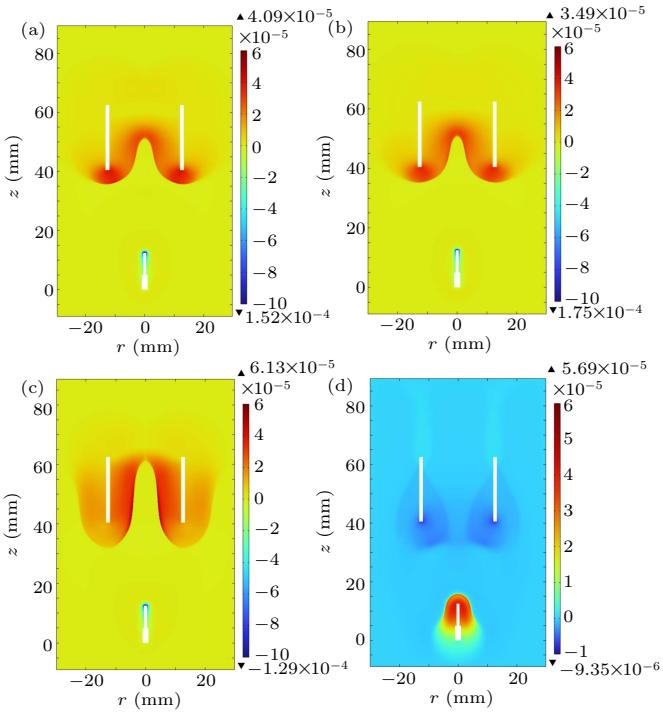


Fig. 7. The spatial distribution of charge density (in unit C/m^3) at (a) $V_e = 3$ kV, $\gamma = 0.01$, $\zeta = 4:1$; (b) $V_e = 3$ kV, $\gamma = 0.01$, $\zeta = 5:1$; (c) $V_e = 3$ kV, $\gamma = 0.001$, $\zeta = 4:1$; (d) $V_e = -3$ kV, $\gamma = 0.01$, $\zeta = 4:1$.

The spatial distribution of charge density in the negative corona discharge is shown in Fig. 7(d). Since the collector electrode has a higher electric potential than the emitter electrode, the data show that positive charges predominate in the ionization region, while negative charges accumulate in the drift region. Furthermore, compared to the positive corona discharge in Fig. 7(a), the ionization region occupies a broader area in the negative corona discharge, and the peak charge

density in the drift region is reduced by 77.13% (as shown in Fig. 8(d)). Two primary mechanisms underlie these phenomena: First, when the voltage polarity is switched to negative corona discharge, the positive ion reaction rate increases significantly along the z-axis in the range of 12.7 mm–17 mm (see the curves for cases 1 and 4 in Fig. 8(a)). Second, the negative ion reaction rate in the drift region remains extremely low (see the lines for cases 1 and 4 in Fig. 8(b)) and are maintained below 1×10^{17} (1/(m^3·s)).

As shown in Fig. 8, the ion reaction rates near the emitter and collector electrodes are significantly higher than those in other regions of the thruster, a trend consistent with previous studies.[24,30,37] This phenomenon can be attributed to three key factors: (i) as listed in Table 1, half of the chemical reactions in air corona discharge involve electron energy; (ii) electron energy is primarily derived from the local electric field; (iii) the emitter and collector electrodes exhibit the strongest electric fields within the thruster, which arises from their highly curved surfaces.

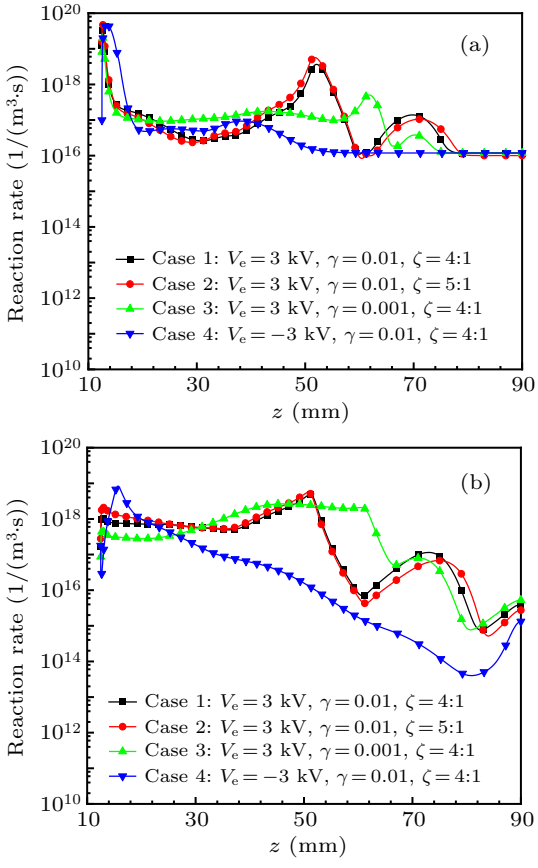


Fig. 8. The ions rates along the axis of the EHD thruster: (a) positive ion, (b) negative ion.

The electric field values along the axis of the EHD thruster are displayed in Fig. 9 in order to ascertain the effects of charged species on the electric fields based on Eqs. (18) and (24). As shown in the curve of case 1 in Fig. 9, the electric field in the positive corona discharge has three peaks ($z = 12.5$ mm, 54.8 mm, and 67.2 mm), with the first peak (appearing on the emitter electrode surface) being the largest. The largest electric field value can be decreased from 3.17×10^4 V/m to 2.39 V/m$\times 10^4$ V/m with the ζ is varied from 4:1 to 5:1 as indicated in the curves of case 1 and case 2 in Fig. 9. Moreover, the electric field exhibits significant fluctuations at $z = 50$ mm–60 mm in the curves of case 1 and case 2 in Fig. 9, because the electric field raises with the increase of charge density (see Eqs. (18) and (19)) and the high charge density around the axis of collector electrode (see Figs. 7(a) and 7(b)).

It can be observed from the graph of case 1 and 3 in Fig. 9 that the maximum electric field value remains on the surface of the emitter electrode. However, when the SEEC is reduced from 0.01 to 0.001, both the second and third local peaks shift toward the $+z$ direction. Specifically, the second local peak ($z = 63.1$ mm) decreases by 61.8%, and the third local peak ($z = 69.8$ mm) reduces by 64.8%.

Compared with the positive corona discharge (see the line of case 1 in Fig. 9), the negative corona discharge (see the curve of case 4 in Fig. 9) exhibits only two local peaks ($z = 12.5$ mm, 40.1 mm). In addition, the largest electric field value is increased by 82.86%, and the electric field values along the z-axis in the range of 5090 mm are reduced distinctly, as the polarity of voltage is turned to the negative corona discharge.

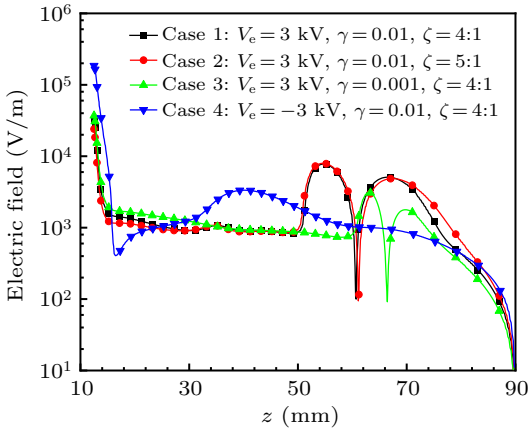


Fig. 9. The electric field values along the axis of the EHD thruster.

The distribution of charged particles and electric field are significantly influenced by the operating settings of the EHD thruster, which alter the electric field forces and current properties. Notably, the ionization region in negative corona discharge exhibits an order-of-magnitude expansion compared to that in positive corona discharge. This disparity becomes particularly pronounced under conventional atmospheric pressure conditions,[22] resulting in parameter-dependent variations in propulsion performance of EHD thrusters.

3.2. The characteristics of propulsion performance

Based on the charge distribution and electrostatic field analysis in Subsection 3.1, figure 10 depicts the spatial distribution of electric field force density for various parameters.

The vector arrows in Fig. 10(a) indicate that the electric field forces in the drift region are consistently directed toward the collector electrode, thereby driving positive ions toward the outlet.

By comparing Fig. 10(a) with Fig. 10(b), it can be observed that the maximal electric field force density in the drift region decreases from 51.8 N/m^3 to 43.7 N/m^3 as the ζ varies from 4:1 to 5:1. However, the spatial distribution of electric field force density in most regions of the EHD thruster remains nearly unchanged.

In comparison to Fig. 10(a), when the SEEC is reduced to 0.001, the electric field force density near the thruster's z-axis approaches to zero, as illustrated in Fig. 10(c). Additionally, the regions where charged species exert force migrate closer to the surface of the collector electrode.

The spatial distribution of electric field force density under negative corona discharge is presented in Fig. 10(d). As clearly shown, the maximum electric field force density in the ionization region reaches 115 N/m^3 , which is more than twice the value observed in positive corona discharge (Fig. 10(a)). Furthermore, a distinct region of intense electric field force density is evident near the emitter electrode.

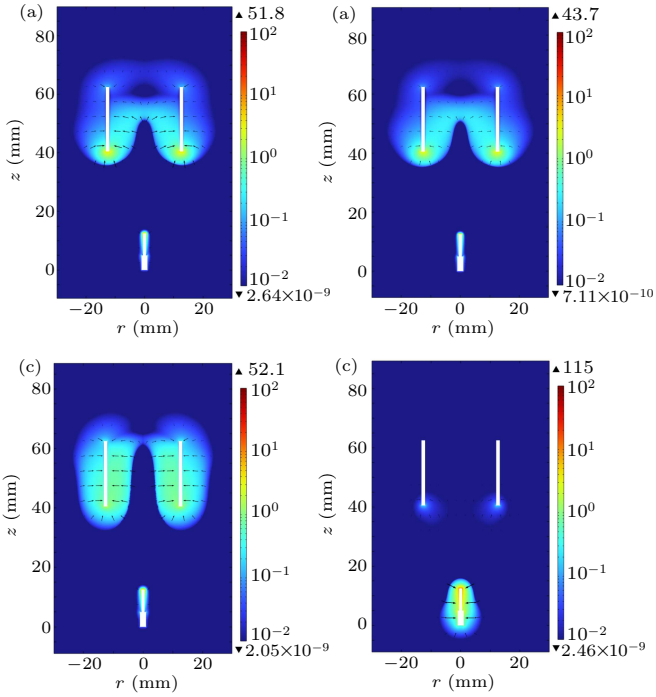


Fig. 10. The spatial distribution of electric field force density (in unit N/m^3) at (a) $V_e = 3$ kV, $\gamma = 0.01$, $\zeta = 4:1$; (b) $V_e = 3$ kV, $\gamma = 0.01$, $\zeta = 5:1$; (c) $V_e = 3$ kV, $\gamma = 0.001$, $\zeta = 4:1$; (d) $V_e = -3$ kV, $\gamma = 0.01$, $\zeta = 4:1$.

The electric field force acting on charged species is a body force within the airflow according to Eqs. (23) and (24). As a result, this force has the ability to change air velocity. The spatial distribution of velocity for various parameters is given in Fig. 11. As shown in Fig. 11(a), the velocity values near the collector electrode axis are higher than those in other regions of the EHD thruster during positive corona discharge. This is because the force regions of the airflow around the collector electrode axis are broader than those in the ionization region (see Fig. 10(a)).

From Figs. 11(a) and 11(b), it is seen that the distribution of velocity remains unaffected by ζ, because the electric field force distribution maintains consistency throughout most regions of the EHD thruster (see Figs. 10(a) and 10(b)). Hence, only the current values exhibit measurable alterations.

A circular, low-speed zone appears at the top of the collector electrode as SEEC drops from 0.01 to 0.001, lowering the outflow velocity from 4.88 cm/s to 4.23 cm/s, as can be seen by comparing Figs. 11(a) and 11(c). The underlying cause lies in the specific electric field force density distribution near the collector electrode as given in Fig. 10(c).

In the case of negative corona discharge as shown in Fig. 11(d), the outlet velocity measures only 0.25 cm/s, which is significantly lower than that observed in positive corona discharge (see Fig. 11(a)). This phenomenon can be interpreted as the body force surrounding the emitter electrode substantially impeding airflow toward the outlet when the voltage polarity is reversed from positive to negative corona discharge (as illustrated in Fig. 10(d)).

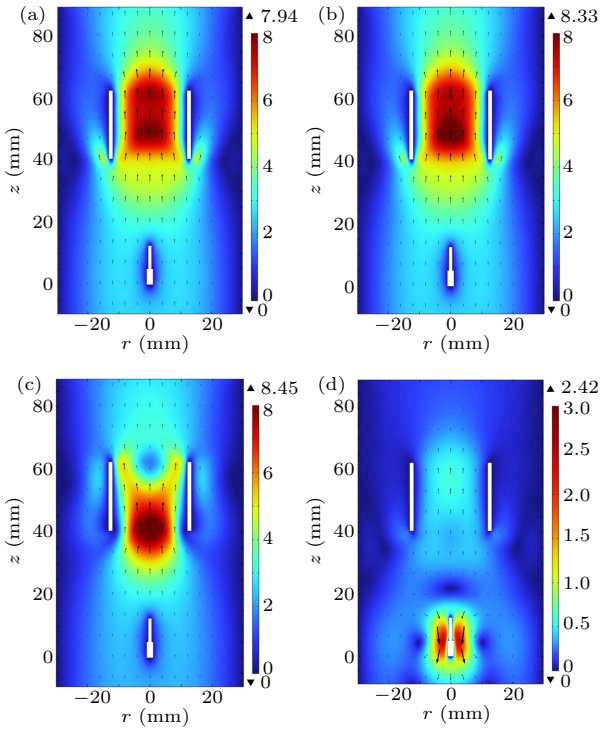


Fig. 11. The spatial distribution of velocity (in unit cm/s) at (a) $V_e = 3$ kV, $\gamma = 0.01$, $\zeta = 4:1$; (b) $V_e = 3$ kV, $\gamma = 0.01$, $\zeta = 5:1$; (c) $V_e = 3$ kV, $\gamma = 0.001$, $\zeta = 4:1$; (d) $V_e = -3$ kV, $\gamma = 0.01$, $\zeta = 4:1$.

The propulsion performance of the EHD thruster under various parameters can be evaluated using velocity distribution results (Fig. 11) and charged species distribution results (Fig. 7), as summarized in Table 7. For cases 1 and 2, although the thrust remains unchanged when the parameter ζ is adjusted from 4:1 to 5:1, the current decreases from 2.44×10^{-3} mA to

1.79×10^{-3} mA. Moreover, the thrust-to-power ratio increases from 29.38 mN/kW to 41.52 mN/kW. This enhancement arises because the thrust-to-power ratio depends on current, thrust, and electrode voltage, as defined in Eq. (26).

The thrust is raised by 34.5% and the thrust-to-power ratio is improved by 142.2% when the SEEC is increased from 0.001 to 0.01 as given in the results of case 1 and case 3 in Table 7.

Table 7. The propulsion performance of EHD thruster under various parameters.

	Thrust (nN)	Current (mA)	Thrust-to-power ratio (mN/kW)
Case 1	13.85	2.44×10^{-3}	29.38
Case 2	13.73	1.79×10^{-3}	41.52
Case 3	10.29	3.56×10^{-3}	12.13
Case 4	00.08	1.50×10^{-3}	00.23

For negative corona discharge, both the thrust and thrust-to-power ratio are only 0.57% and 0.78% of those in positive corona discharge (see cases 1 and 4 in Table 7), respectively. This significant reduction stems from two factors: reversed airflow patterns near the emitter electrode and diminished electric field force density around the collector electrode.

4. Conclusion and perspectives

In this research, a plasma chemical model is used to simulate the EHD thruster with a needle-ring electrode, and the influences of oxygen concentration, SEEC and voltage polarity on its propulsion performance are systematically investigated.

(i) For positive corona discharge, a decrease in oxygen concentration reduces the current and enhances the thrust-to-power of EHD thruster. Compared that with $\zeta = 4:1$, when ζ increases to 5:1, the current decreases by 26.6%, while the thrust and electrode voltage remain nearly unchanged. Notably, the thrust-to-power ratio increases by 41.3%.

(ii) A larger SEEC is more conducive to improving thruster performance under positive corona discharge. When SEEC increases from 0.001 to 0.01, the thrust rises by 34.5%, and the thrust-to-power ratio increases significantly by 142.2%.

(iii) In a low-pressure environment (10 Torr), positive and negative corona discharges exhibit distinct characteristics. For negative corona discharge, the broader ionization region compared to positive corona discharge significantly impedes airflow toward the outlet. Consequently, both thrust and thrust-to-power ratio are less than 1% of those under positive corona discharge. To enhance negative corona discharge performance in future work, we aim to reduce the ionization region by introducing an intermediate electrode near the emitter. Additionally, the performance of series/parallel-configured EHD thrusters under low pressure warrants further investigation.

Acknowledgement

Project supported by the Aeronautical Science Foundation of China (Grant No. 2023Z037052002).

References

[1] Lev D, Myers R M, Lemmer K M, Kolbeck J, Koizumi H and Polzin K 2019 *Acta Astronaut.* **159** 213
[2] Cervone A, Mancas A and Zandbergen B 2015 *Acta Astronaut.* **108** 30
[3] Huh J, Seo D and Kwon S 2017 *Sens Actuators A Phys.* **263** 332
[4] Quan R H, Wang B and Yao Y J. 2023 *Chin. Phys. B* **32** 065201
[5] Masuyama K and Barrett S R H 2013 *Proc. R. Soc. A* **469** 20120623
[6] van Wynsberghe E and Turak A 2016 *Acta Astronaut.* **128** 616
[7] Christenson E A and Moller P S 1967 *AIAA J.* **5** 1768
[8] Xu H, He Y, Strobel K L, Gilmore C K, Kelley S P, Hennick C C and Barrett S R H 2018 *Nature* **563** 532
[9] Khomich V Y, Malanichev V E and Rebrov I E 2021 *Acta Astronaut.* **180** 141
[10] Monrolin N, Plouraboué F and Praud O 2017 *AIAA J.* **55** 4296
[11] Cabanas M F, González F P, González A S, García M R and Melero M G 2022 *Appl. Sci.* **12** 2997
[12] Peng Y H, Li D Z, Yang X Y, Ma Z S and Mao Z B 2023 *Micromachines* **14** 321
[13] Drew D S and Pister K S J 2017 *Micromachines* **8** 141
[14] Zhang G W, Yang J K and Lin X H 2021 *Chin. Phys. B* **30** 014701
[15] Leng J, Liu Z, Zhang X, Huang D, Huang J, Qi M and Yan X 2021 *IOP Conference Series: Earth and Environmental Science* **675** 012015
[16] Rickard M and Dunn-Rankin D 2007 *J. Electrostat.* **65** 646
[17] Rickard M, Dunn-Rankin D, Weinberg F and Carleton F 2006 *J. Electrostat.* **64** 368
[18] Granados V H, Pinheiro M J and Sá P A 2016 *Phys. Plasmas* **23** 073514
[19] Fang J, Zhang Y, Lu C, Gu L, Xu S, Guo Y and Shi J 2024 *Chin. Phys. B* **33** 015201
[20] Granados V H, Pinheiro M J and Sá P A 2017 *Phys. Plasmas* **24** 123513
[21] Granados V H, Pinheiro M J and Sá P A 2017 *Phys. Plasmas* **24** 093508
[22] Guan Y, Vaddi R S, Aliseda A and Novosselov I 2018 *Phys. Rev. Fluids* **3** 043701
[23] Gu L, Tan W, He J, Jiang Z, Chen X, Ren W and Jin Z 2023 *Energies* **16** 5257
[24] Mahadevan S and Raja L L 2010 *J. Appl. Phys.* **107** 093304
[25] Carbone E, Graef W and Hagelaar G 2021 *Atoms* **9** 16
[26] Hagelaar G J M and Pitchford L C 2005 *Plasma Sources Sci. Technol.* **14** 722
[27] Zhao Z, Wei X, Guan R, Nie H, Zhu B and Yao Y 2022 *IEEE Trans. Plasma Sci.* **50** 1160
[28] Morrow R and Sato N 1999 *J. Phys. D: Appl. Phys.* **32** L20
[29] Bedolla P O, Vorlaufer G, Sequard-Base P, Vernes A and Franek F 2017 *J. Electrostat.* **87** 32
[30] Liu K L, Liao R J and Zhao X T 2015 *J. Electr. Eng. Technol.* **10** 1804
[31] Liu X H, He W, Yang F, Wang H Y, Liao R J and Xiao H G 2012 *Chin. Phys. B* **21** 075201
[32] Wu F F, Liao R J, Wang K, Yang L J and Grzybowski S 2014 *IEEE Trans. Plasma Sci.* **42** 868
[33] Chen S, Nobelen J C and Nijdam S 2017 *Plasma Sources Sci. Technol.* **26** 095005
[34] Li X C, Wan W J, Liu X Q, Chen M, Wu K Y, Ran J X and Sun H 2024 *Chin. Phys. B* **34** 035202
[35] Tran T N, Golosnoy I O, Lewin P L and Georghiou G E 2010 *J. Phys. D: Appl. Phys.* **44** 015203
[36] Viehland L A and Mason E A 1995 *At. Data Nucl. Data Tables.* **60** 37
[37] Sima W, Peng Q and Yang Q 2012 *IEEE Trans. Dielectr. Electr. Insul.* **19** 660